A Novel Harmonic State-space Modelling Method on the Modular Multilevel Matrix Converter and Coupling Analysis

Jing Li, *Member*, *CSEE*, Boyang Zhao, *Member*, *IEEE*, Shenquan Liu, *Member*, *IEEE*, *Member*, *CSEE*, Jie Li, Xiuli Wang, *Senior Member*, *IEEE*, *Member*, *CSEE*, and Xifan Wang, *Life Fellow*, *IEEE*, *Fellow*, *CSEE*

***Abstract*—The fractional frequency transmission system is an emerging technology for long-distance wind power integration, and the modular multilevel matrix converter (M^3C) is the keen equipment. Since the M^3C directly connects two ac grids with different frequencies, the external and internal harmonics have complex coupling relationships with a unique dual-fundamental-frequency spectrum, which has not been properly investigated due to a lack of an effective method. To address this issue, a novel harmonic state-space method is proposed to achieve comprehensive modelling of the harmonic dynamics of the M^3C. Based on the principle of two-dimensional Fourier transform, the decomposition of the dual-fundamental-frequency harmonics is realized, and the multiplicative coupling between time-domain variables is modelled through double-layer convolution on the frequency domain. Besides, the general expression of the proposed method is provided, which highlights a modularized matrix with easy scalability to meet different truncation requirements. Then, the HSS model of M^3C considering the close-loop control is established, based on which a panoramic harmonic coupling relationship between the system- and the low-frequency side is concluded. Finally, the M^3C model and harmonic coupling relationship are validated by simulation tests conducted in MATLAB/Simulink environment.**

***Index Terms*—Harmonic state-space, harmonic transmission, modular multilevel matrix converter.**

I. Introduction

THE Fractional Frequency Transmission System (FFTS), which is usually referred to as low-frequency ac transmission, is an emerging solution to long-distance offshore wind farms [1], [2]. The principle of FFTS is to boost the transmission capacity, efficiency, and distance of ac submarine cables [3] by lowering the power frequency, e.g., from 50 or 60 Hz to 50/3 or 20 Hz. The frequency converter is the most important equipment in the FFTS. The Modular Multilevel Converter technology is favored to meet the high-voltage and bulky-power power conversion requirements, and the modular multilevel matrix converter (M^3C) proposed in [4] is generally recognized as the most promising topology due to higher efficiency, reliability, and economy performance [5]–[7].

Due to its considerable application potential, modelling and control of the M^3C have been intensively investigated in the past years. Compared with the AC/DC MMC, the M^3C has a more complex nine-arm topology that connects two AC systems with distinct frequencies [4], which makes its internal dynamics extremely complex. To handle the topological challenge, the double $\alpha\beta0$ transformation is a popular method for circuit analysis of the M^3C, which successfully separates the system-side, low-frequency-side (LF-side) and inner circulating electrical quantities [8], [9]. Based on the double $\alpha\beta0$ transformation, subsequent research proposed the decoupled control strategies [10]–[12], including capacitor voltage balancing control, grid-tied power control, and circulating current suppression, etc. On the other hand, the fundamental-frequency voltage and current from the input- and output-sides will couple with each other inner the M^3C circuit, generating a series of SM capacitor voltage ripples and arm current harmonics [13], [14]. These ripple/harmonic series follow a unique dual-fundamental-frequency spectrum centering two AC grid frequencies. Since the double-$\alpha\beta0$ transformation is less straightforward in the description of the multiplicative coupling between variables among the arms, literature [15] proposed the two-dimensional (2-D) phasor method to achieve fast determination of the characteristics of high-order inner-M^3C electrical variables.

Although the M^3C is claimed to be capable of decoupled operation on the system side and the LF-side, the controller is designed under the ideal grid assumption [10]–[12], i.e., the system- and LF-side three-phase grids only contain the fundamental-frequency positive-sequence voltages and currents. Therefore, the so-called "decoupled operation capability" is specifically suitable for the ideal grid conditions. Nevertheless, in the field, the power grid is undergoing continuous perturbations that inevitably introduce background harmonics, especially for modern power grids with high power-electronics penetration ratio [16], [17]. These background harmonics will

Manuscript received January 15, 2024; revised March 25, 2024; accepted April 29, 2024. Data of online publication July 24, 2024; data of current version November 7, 2024. This work was supported by the National Natural Science Foundation of China (52207103) and in part by Basic and Appiled Basic Research Foundational of Guangdong Province (2020A1515111117).

J. Li, B. Y. Zhao, X. L. Wang and X. F. Wang are with school of Electrical Engineering, Xi'an Jiaotong University and Shaanxi Key Laboratory of Smart Grid in Xi'an Jiaotong University, Xi'an, 710049, China.

S. Q. Liu (corresponding author, email: liushenquan.1990@gmail.com; ORCID: https://orcid.org/0000-0001-5568-9288) and J. Li are with school of Electric Power Engineering, South China University of Technology, Guangzhou 510641, China.

DOI: 10.17775/CSEEJPES.2024.00370

break the ideal boundary conditions of the M^{3}C, cause changes in inner-coupling characteristics and finally, may arouse additional grid-tied harmonics on both sides that deteriorate power quality and threaten the power safety [18].

However, this harmonic coupling mechanism and characteristics of the M^{3}C are rarely discussed in existing research. Investigation towards this issue requires comprehensive tracking of the coupling relationship between the external and internal electrical quantities, which can be extremely challenging considering the dual-fundamental-frequency spectrum of the M^{3}C. The dynamic phasor [19], [20] and Harmonic State-Space (HSS) method are common methods for similar scenarios such as inner dynamic modelling of the AC/DC MMC [21]–[23], which decomposes the time-varying model of sub-module (SM) capacitor voltage and arm current into series non-time-varying models of their Fourier coefficients. Nevertheless, the conventional methods are designed for regular systems with single-fundamental-frequency, and not suitable for the dual-fundamental-frequency harmonic spectrum of the M^{3}C. Besides, a small-signal model with closed-loop control is developed [24], and subsequent steady-state harmonic analysis is performed in [13], which also adopts the principles of the Fourier series. However, the research assumes that the frequency ratio is constant 3:1 (60 Hz for the main grid and 20 Hz for the low-frequency grid) so that 20 Hz can be selected as the common fundamental frequency, which is over-simplified considering the routine frequency fluctuation of power grids.

To address this issue, an improved HSS method is proposed for the dual-fundamental-frequency characteristics of M^{3}C. Based on the principles of the two-dimensional Fourier transform, the decomposition of the dual-fundamental-frequency ripple/harmonic is realized, and the multiplicative coupling on the time domain is modelled through double-layer convolution on the frequency domain, which effectively solves the inner-dynamics modelling problem of M^{3}C. Besides, the proposed method also highlights its modularized matrix structure, which provides easy scalability to meet different model truncation requirements. Then, the HSS model of M^{3}C considering the close-loop control is established, based on which a panoramic harmonic coupling relationship between the system- and LF-side is concluded. Finally, the M^{3}C model and harmonic coupling relationship are validated by simulation tests conducted in MATLAB/Simulink environment.

Compared with the existing research, the main contributions of this paper are provided as follows:

1) The improved method realizes the decomposition of the dual-fundamental-frequency component in the two frequency dimensions based on the principle of the two-dimensional Fourier transform, , and there is no need to consider the ratio relationship between two frequencies, which can effectively realize the mathematical description of the high-order dynamic process the internal of M^{3}C, and clearly depict the cross-coupling process between the state variables of different frequencies and different phase sequences, and depict the influence of its output characteristics;

2) The proposed method can extend the conventional HSS method for a single fundamental frequency system to the dual fundamental frequency coupling scenario of M^{3}C, which can realize the linearization and contactization of the M^{3}C model. Then the small-signal stability of the system can be analyzed by the linear control theory, which can lay the foundation for the resonance stability analysis of the FFTS based on M^{3}C.

The rest of the paper is organized as follows. Section II proposes the improved HSS modelling method with generalized expressions; Section III introduces the M^{3}C configuration and develops the HSS model considering the close-loop control; Section IV reveals the harmonic coupling relationship between the external and the inner dynamics of M^{3}C. Section V verifies the correctness of the modelling method and established model based on MATLAB/Simulink simulations; Section VI concludes the paper.

II. An Improved HSS Method Based on Two-Dimensional Fourier Transform

A. Fundamentals of HSS Method

The HSS method is based on the fundamental theories of linear time-periodic (LTP) systems and harmonic balance, whose core idea is to convert the time-domain multiplication into the frequency-domain convolution [25], [26].

Assume the existence of an arbitrary LTP system:

$$\begin{cases} \dot{\boldsymbol{x}}(t) = \boldsymbol{A}(t)\boldsymbol{x}(t) + \boldsymbol{B}(t)\boldsymbol{u}(t) \\ \boldsymbol{y}(t) = \boldsymbol{C}(t)\boldsymbol{x}(t) + \boldsymbol{D}(t)\boldsymbol{u}(t) \end{cases} \tag{1}$$

where $\boldsymbol{x}(t)$, $\boldsymbol{u}(t)$, and $\boldsymbol{y}(t)$ are state, input and output variables, respectively; $\boldsymbol{A}(t)$, $\boldsymbol{B}(t)$, $\boldsymbol{C}(t)$, and $\boldsymbol{D}(t)$ are time-periodic coefficient matrices of the corresponding variables.

$$\boldsymbol{x}(t) = \mathrm{e}^{st} \sum_{h=-\infty}^{\infty} \boldsymbol{x}_h \mathrm{e}^{\mathrm{j}h\omega_0 t} \tag{2}$$

$$\boldsymbol{x}_h = \frac{1}{T_0} \int_{t-T_0}^{t} \boldsymbol{x}(t) \mathrm{e}^{-\mathrm{j}h\omega_0 t} \tag{3}$$

where e^{st} is an exponential periodic modulated function; ω_0 denotes the fundamental angular frequency; $\boldsymbol{x}_h$ is the h^{th}-order Fourier coefficient of $\boldsymbol{x}(t)$. In addition, $\boldsymbol{u}(t)$ can also be expressed in the form of (2) and (3).

On the other hand, the coefficient matrices, namely $\boldsymbol{A}(t)$, $\boldsymbol{B}(t)$, $\boldsymbol{C}(t)$, and $\boldsymbol{D}(t)$, can also be expressed by their Fourier series:

$$\begin{array}{c:c} \boldsymbol{A}(t) = \sum\limits_{h=-\infty}^{+\infty} \boldsymbol{A}_h \mathrm{e}^{\mathrm{j}h\omega_0 t} & \boldsymbol{B}(t) = \sum\limits_{h=-\infty}^{+\infty} \boldsymbol{B}_h \mathrm{e}^{\mathrm{j}h\omega_0 t} \\ \hdashline \boldsymbol{C}(t) = \sum\limits_{h=-\infty}^{+\infty} \boldsymbol{C}_h \mathrm{e}^{\mathrm{j}h\omega_0 t} & \boldsymbol{D}(t) = \sum\limits_{h=-\infty}^{+\infty} \boldsymbol{D}_h \mathrm{e}^{\mathrm{j}h\omega_0 t} \end{array} \tag{4}$$

By substituting the vectors and matrices in Fourier series form into (1), and the equation for each component can be derived as:

$$\begin{cases} (s + \mathrm{j}n\omega_0)\boldsymbol{x}_{\mathrm{n}} = \sum\limits_{m\in Z} \boldsymbol{A}_{n-m}\boldsymbol{x}_m + \sum\limits_{m\in Z} \boldsymbol{B}_{n-m}\boldsymbol{u}_m \\ \boldsymbol{y}_{\mathrm{n}} = \sum\limits_{m\in Z} \boldsymbol{C}_{n-m}\boldsymbol{x}_m + \sum\limits_{m\in Z} \boldsymbol{D}_{n-m}\boldsymbol{u}_m \end{cases} \tag{5}$$

The HSS model can be obtained by assembling all the sub-models of frequency components within h^{th}-order truncation in the following form:

$$\begin{cases} s\boldsymbol{X} = (\Gamma(\boldsymbol{A}) - \boldsymbol{N})\boldsymbol{X} + \Gamma(\boldsymbol{B})\boldsymbol{U} \\ \boldsymbol{Y} = \Gamma(\boldsymbol{C})\boldsymbol{X} + \Gamma(\boldsymbol{D})\boldsymbol{U} \end{cases} \tag{6}$$

where $\boldsymbol{X}$, $\boldsymbol{Y}$ and $\boldsymbol{U}$ represent the harmonic coefficients of $\boldsymbol{x}(t)$, $\boldsymbol{y}(t)$ and $\boldsymbol{u}(t)$, respectively; Taking $\boldsymbol{X}$ as an example, the general expression is:

$$X = [\boldsymbol{x}_{-h}^{\mathrm{T}}, \cdots, \boldsymbol{x}_{-1}^{\mathrm{T}}, \boldsymbol{x}_{0}^{\mathrm{T}}, \boldsymbol{x}_{1}^{\mathrm{T}}, \cdots, \boldsymbol{x}_{h}^{\mathrm{T}}]^{\mathrm{T}} \tag{7}$$

Therefore, the convolution coupling relationship is shown in Fig. 1. $\Gamma(\boldsymbol{A})$, $\Gamma(\boldsymbol{B})$, $\Gamma(\boldsymbol{C})$ and $\Gamma(\boldsymbol{D})$ are Toeplitz matrices composed of the Fourier coefficients of $\boldsymbol{A}(t)$, $\boldsymbol{B}(t)$, $\boldsymbol{C}(t)$ and $\boldsymbol{D}(t)$. Take $(\boldsymbol{A})$ as an example, the generalized form of Toeplitz matrix is expressed by (8);

$$\Gamma(\boldsymbol{A}) = \begin{bmatrix} \boldsymbol{A}_0 & \cdots & \boldsymbol{A}_{-h} & \cdots & \boldsymbol{O} \\ \vdots & \ddots & \vdots & \ddots & \vdots \\ \boldsymbol{A}_h & \cdots & \boldsymbol{A}_0 & \cdots & \boldsymbol{A}_{-h} \\ \vdots & \ddots & \vdots & \ddots & \vdots \\ \boldsymbol{O} & \cdots & \boldsymbol{A}_h & \cdots & \boldsymbol{A}_0 \end{bmatrix}_{a((2h+1)\times(2h+1))} \tag{8}$$

where the subscript represents the matrix size; a represents the number of state variables in the LTP system; the submatrix $\boldsymbol{A}_k (k \in [-h, h])$ is the k^{th}-order Fourier coefficient of $\boldsymbol{A}(t)$; $\boldsymbol{O}$ is the zero matrix.

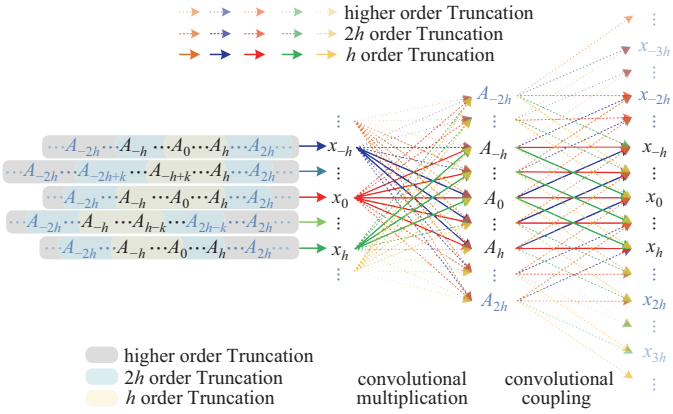

Fig. 1. HSS model convolution relationship.

$\boldsymbol{N}$ is a diagonal matrix containing the frequency domain information.

$$\boldsymbol{N} = \mathrm{diag}(-\mathrm{j}h\omega_0\boldsymbol{I}, \cdots, -\mathrm{j}\omega_0\boldsymbol{I}, \boldsymbol{O}, \mathrm{j}\omega_0\boldsymbol{I}, \cdots, \mathrm{j}h\omega_0\boldsymbol{I}) \tag{9}$$

where $\boldsymbol{I}$ denote the identity matrix of the same order with $\boldsymbol{x}(t)$.

B. Inapplicability of the Conventional HSS Method in Dual-Fundamental-Frequency Scenarios

The conventional HSS modelling method is applicable for most cases because systems with one single fundamental frequency are most common. In these cases, the time-domain signal can be transformed into the superposition of a series of frequency components with the integral multiple of the fundamental frequency.

However, if another fundamental-frequency series exists, to establish the HSS model, the greatest common divisor (GCD) of the two fundamental frequencies should be selected as the common fundamental frequency. Fig. 2(a) shows the selection of GCD fundamental-frequency (f_{GCD}) for typical two fundamental-frequency systems. In *cases* 1, 2 and 3, the first fundamental frequency is 50 Hz, while the second fundamental frequency is 20 Hz, 50/3 Hz and 19 Hz, respectively, to mimic potential fluctuation in power systems. Consequently, f_{GCD} equals 10 Hz, 50/3 Hz and 1 Hz, respectively.

Although the HSS model can still be established, this solution will arouse several problems that hinder further analysis. The first problem is the rapidly growing model scale. In *cases* 1, 2 and 3, the 50 Hz component locates on the 5^{th}-, 3^{rd}- and 50^{th}-order, respectively. The model order must become much larger if a suitable f_{GCD} cannot be found [27]. Another more serious problem is the varying model structure. The distribution of the frequency series will change under different f_{GCD}, which alters the model structure. Considering that frequency fluctuation is common in power systems, it is difficult to establish a conventional HSS model to cover all scenarios.

C. Improved HSS Method Based on Two-Dimensional Fourier Transform

To address this issue, an improved HSS method is proposed based on the principle of the two-dimension Fourier transform. For a time-domain dual-fundamental-frequency periodic state matrix $\boldsymbol{x}(t)$, it can be expressed by the two-dimension Fourier series as:

$$\boldsymbol{x}(t) = \sum_{k_1=-\infty}^{+\infty} \sum_{k_2=-\infty}^{+\infty} \boldsymbol{X}_{k_1,k_2} \mathrm{e}^{st} \mathrm{e}^{\mathrm{j}(k_1\omega_1 + k_2\omega_2)t} \tag{10}$$

where ω_1 and ω_2 are the fundamental frequencies of two independent AC systems, respectively; $\boldsymbol{X}_{k_1,k_2}$ is the two-dimensional Fourier coefficient, and k_1 and k_2 are the orders to the corresponding fundamental frequencies, respectively.

Figure 2(b) shows the distribution of frequency components under two-dimension Fourier decomposition. The components are now distributed on the $f_{\text{S}} - f_{\text{L}}$ panel instead of a single axis. The varying second fundamental frequency in *cases* 1, 2 and 3 is simply represented by different f_{L}, which also avoids the changing model structure problem. The model order will not increase too much. Consequently, this method can achieve more reasonable component decomposition of double-fundamental-frequency signals and thereby, can realize the independent, flexible, and adjustable modelling for the double-fundamental-frequency systems.

By substituting (10) into (1), the state-space equation of the (k_1^{th}, k_2^{th})-order dual-fundamental-frequency coefficient can be obtained:

$$(s + jk_1\omega_1 + jk_2\omega_2)\boldsymbol{x}_{k_1,k_2} = \sum_{m\in Z} \sum_{l\in Z} \boldsymbol{A}_{k_1-m,k_2-l}\boldsymbol{x}_{m,l}$$

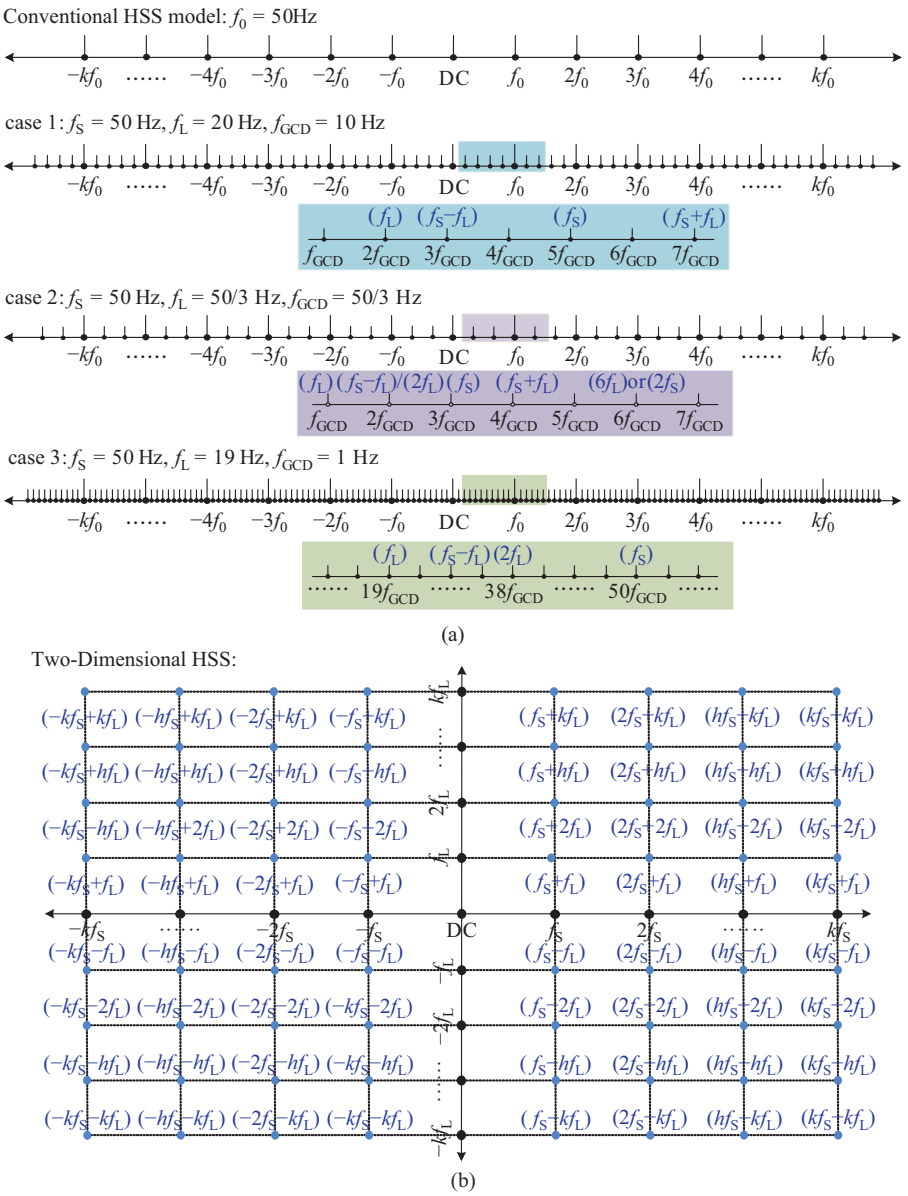

Fig. 2. Distinctive of one-dimensional and two-dimensional for dual-fundamental-frequency system. (a) One-dimensional modelling. (b) Two-dimensional modelling.

$$+\sum_{m\in Z}\sum_{l\in Z}\boldsymbol{B}_{k_1-m,k_2-l}\boldsymbol{u}_{m,l}$$
$$\boldsymbol{y}_{k_1,k_2}=\sum_{m\in Z}\sum_{l\in Z}\boldsymbol{C}_{k_1-m,k_2-l}\boldsymbol{x}_{m,l}$$
$$+\sum_{m\in Z}\sum_{l\in Z}\boldsymbol{D}_{k_1-m,k_2-l}\boldsymbol{u}_{m,l} \tag{11}$$

In addition, the unified harmonic order h for a dual-fundamental-frequency system is defined as:

$$h\triangleq|k_1|+|k_2| \tag{12}$$

and the h^{th}-order truncated model contains all the harmonic components of $\{(k_1,k_2)||k_1|+|k_2|\le h\}$. Consequently, the area covered by the h^{th}-order truncated model is a lozenge on the k_1–k_2 panel, as is presented in Fig. 3.

In the proposed modelling method, the two-fundamental-frequency HSS model shares the generalized formation of that in (6), which is expressed as:

$$\begin{cases} s\boldsymbol{X}_{\text{df}}=(\boldsymbol{A}_{\text{df}}-\boldsymbol{N}_{\text{df}})\boldsymbol{X}_{\text{df}}+\boldsymbol{B}_{\text{df}}\boldsymbol{U}_{\text{df}} \\ \boldsymbol{Y}_{\text{df}}=\boldsymbol{C}_{\text{df}}\boldsymbol{X}_{\text{df}}+\boldsymbol{D}_{\text{df}}\boldsymbol{U}_{\text{df}} \end{cases} \tag{13}$$

where the subscript df represents the dual-fundamental-frequency HSS model.

Nevertheless, the structure of the vectors and matrices are different to fit the dual-fundamental-frequency spectrum. The vectors, namely $\boldsymbol{X}_{\text{df}}$, $\boldsymbol{U}_{\text{df}}$ and $\boldsymbol{Y}_{\text{df}}$, share the same structure. Taking $\boldsymbol{X}_{\text{df}}$ as an example, the general expression for $\boldsymbol{X}_{\text{df}}$ is expressed by:

$$\boldsymbol{X}_{\text{df}}=[\boldsymbol{x}^{\text{T}}_{-h,(:)}\ \cdots\ \boldsymbol{x}^{\text{T}}_{-1,(:)}\ \boldsymbol{x}^{\text{T}}_{0,(:)}\ \boldsymbol{x}^{\text{T}}_{1,(:)}\ \cdots\ \boldsymbol{x}^{\text{T}}_{h,(:)}]^{\text{T}} \tag{14}$$

where $\boldsymbol{x}_{n,(:)}(n\in[-h,h])$ represents the assembly of coefficients with the same order of n on the ω_1 dimension ranging

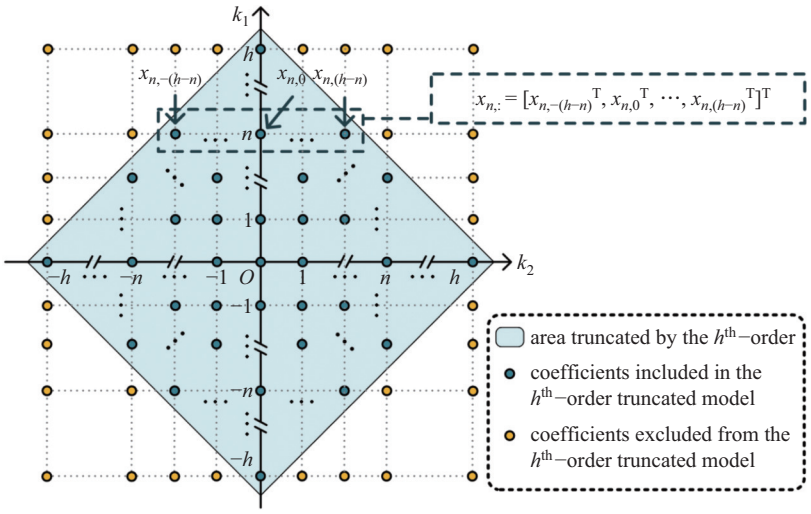

Fig. 3. Diagram of the coefficients included in the h^{th}-order truncated model.

from $\boldsymbol{x}_{n,-(h-|n|)}$ to $\boldsymbol{x}_{n,(h-|n|)}$, including $[2(h-|n|)+1]$ elements. In Fig. 3, $\boldsymbol{x}_{n,(:)}$ denotes all the truncated elements on the same row intercepting at $k_1=n$. Therefore, $\boldsymbol{x}_{n,(:)}$ can be further expanded as:

$$\boldsymbol{x}_{n,(:)}=\underbrace{[\boldsymbol{x}_{n,-(h-|n|)}^{\mathrm{T}} \quad \cdots \quad \boldsymbol{x}_{n,-1}^{\mathrm{T}} \quad \boldsymbol{x}_{n,0}^{\mathrm{T}} \quad \boldsymbol{x}_{n,1}^{\mathrm{T}} \quad \cdots \quad \boldsymbol{x}_{n,(h-|n|)}^{\mathrm{T}}]^{\mathrm{T}}}_{\text{size:}[(2h-2|n|+1)a]\times 1} \tag{15}$$

where the size of $\boldsymbol{x}_{n,(:)}$ is marked below with a representing the dimension of $\boldsymbol{x}(t)$. Consequently, the size of $\boldsymbol{X}_{\mathrm{df}}$ can be calculated as $[(2h^2+2h+1)a]\times 1$. In addition, $\boldsymbol{U}_{\mathrm{df}}$ and $\boldsymbol{Y}_{\mathrm{df}}$ also share the structure defined by (14) and (15).

The matrices, namely, $\boldsymbol{A}_{\mathrm{df}}$, $\boldsymbol{B}_{\mathrm{df}}$, $\boldsymbol{C}_{\mathrm{df}}$ and $\boldsymbol{D}_{\mathrm{df}}$, also share the same structure. The double-layer convolution can be also represented by the double-layer Toeplitz matrices obtained via dual expansions on the ω_1 and ω_2 dimensions. Taking $\boldsymbol{A}_{\mathrm{df}}$ as an example, the first-layer expansion is expressed by:

$$\boldsymbol{A}_{\mathrm{df}}=\underbrace{\begin{bmatrix} \boldsymbol{A}_{0,(:)}^{(-h)} & \cdots & \boldsymbol{A}_{-h,(:)}^{(-h)} & \cdots & \boldsymbol{O} \\ \vdots & \ddots & \vdots & \ddots & \vdots \\ \boldsymbol{A}_{h,(:)}^{(0)} & \cdots & \boldsymbol{A}_{0,(:)}^{(0)} & \cdots & \boldsymbol{A}_{-h,(:)}^{(0)} \\ \vdots & \ddots & \vdots & \ddots & \vdots \\ \boldsymbol{O} & \cdots & \boldsymbol{A}_{h,(:)}^{(h)} & \cdots & \boldsymbol{A}_{0,(:)}^{(h)} \end{bmatrix}}_{\text{size:}(2h^2+2h+1)a\times(2h^2+2h+1)a} \tag{16}$$

where $\boldsymbol{A}_{n,(:)}^{(p)}(n,p\in[-h,h])$ represents the state-transition matrix on the ω_1 dimension, while p symbolizes the ω_2-dimension sequences unexpanded in the two-dimensional framework. Although (16) and (8) have similar structures, the sub-matrices in (16) have different sizes due to the varying length of $\boldsymbol{x}_{n,(:)}(n\in[-h,h])$. The submatrix $\boldsymbol{A}_{n,(:)}^{(p)}$ connects $\boldsymbol{x}_{p-n,(:)}$ to $s\boldsymbol{x}_{p,(:)}$, i.e.:

$$\underbrace{s\boldsymbol{x}_{p,(:)}}_{(2h-2|p|+1)a\times 1} \leftarrow \underbrace{\boldsymbol{A}_{n,(:)}^{(p)}}_{\substack{(2h-2|p|+1)a \\ \times(2h-2|p-n|+1)a}} \cdot \underbrace{\boldsymbol{x}_{p-n,(:)}}_{(2h-2|p-n|+1)a\times 1} \tag{17}$$

Consequently, the size of $\boldsymbol{A}_{n,(:)}^{(p)}$ is determined by both p and n, and will change in different rows. By substituting (14) into (17), $\boldsymbol{A}_{n,(:)}^{(p)}$ can be further expanded as:

$$\boldsymbol{A}_{n,(:)}^{(p)}=\begin{bmatrix} \boldsymbol{A}_{n,(|p|-|n-p|)} & \cdots & \boldsymbol{A}_{k_1,-(h-|p|)} & \cdots & \boldsymbol{O} \\ \vdots & \ddots & \vdots & \ddots & \vdots \\ \boldsymbol{A}_{n,(h-|n-p|)} & \cdots & \boldsymbol{A}_{n,0} & \cdots & \boldsymbol{A}_{n,-(h-|n-p|)} \\ \vdots & \ddots & \vdots & \ddots & \vdots \\ \boldsymbol{O} & \cdots & \boldsymbol{A}_{n,(h-|p|)} & \cdots & \boldsymbol{A}_{n,-(|p|-|n-p|)} \end{bmatrix} \tag{18}$$

where $\boldsymbol{A}_{k_1,k_2}$ denotes the $(k_1^{\mathrm{th}},k_2^{\mathrm{th}})$-order coefficient of $\boldsymbol{A}(t)$.

In addition, $\boldsymbol{N}_{\mathrm{df}}$ can be expressed by:

$$\begin{aligned}\boldsymbol{N}_{\mathrm{df}}=\mathrm{diag}(&\boldsymbol{N}_{-h,(:)} \quad \cdots \quad \boldsymbol{N}_{-1,(:)} \quad \boldsymbol{N}_{0,(:)} \\ &\boldsymbol{N}_{1,(:)} \quad \cdots \quad \boldsymbol{N}_{h,(:)})\end{aligned} \tag{19}$$

where $\boldsymbol{N}_{n,(:)},n\in[-h,h]$ represents the coefficients on the ω_1 dimension, which shall be further expanded on the ω_2 dimension:

$$\begin{aligned}\boldsymbol{N}_{n,(:)}=\mathrm{diag}(&\mathrm{j}(n\omega_1-(h-|n|)\omega_2)\boldsymbol{I},\cdots,\mathrm{j}(n\omega_1-\omega_2)\boldsymbol{I}, \\ &\mathrm{j}n\omega_1\boldsymbol{I},\mathrm{j}(n\omega_1+\omega_2)\boldsymbol{I},\cdots,\mathrm{j}(n\omega_1+(h-|n|)\omega_2)\boldsymbol{I})\end{aligned} \tag{20}$$

III. HSS Model of M^{3}C Considering Close-Loop Control

A. M^3C Configuration

For simplified description, in the rest of this paper, i will represent any phase-terminal of the LF-side, i.e., phase-terminal a, b, and c; while j will represent any phase-terminal of the system-side, i.e., phase-terminal u, v, and w.

Figure 4 shows the configuration of M^{3}C. The M^{3}C contains nine arms to achieve full connection between the phase-terminal groups $\{a,b,c\}$ and $\{u,v,w\}$. Each arm is named according to the terminals at its two ends, such as arm au, bw, cv, *etc*, which contains n series-connected full-bridge

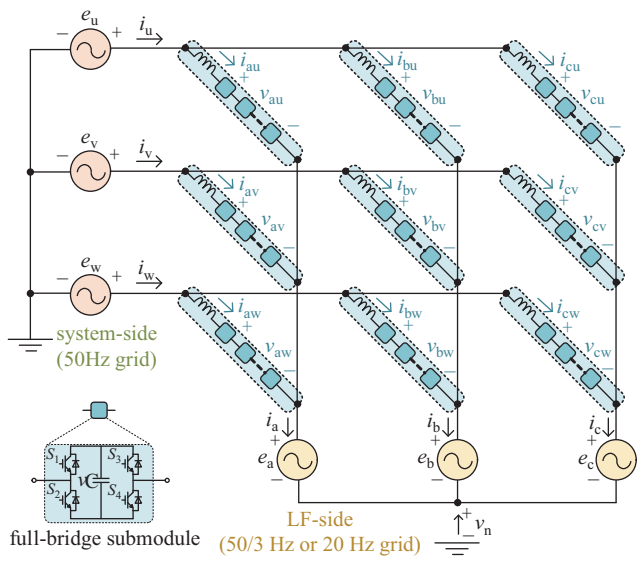

Fig. 4. Configuration of M^{3}C.

SMs (FBSMs) and an inductor L. Ignoring the SM capacitor voltage variance, each FBSM stack can output $(2N+1)$ voltage levels ranging from $-Nv_{\mathrm{C}}$ to Nv_{C} according to the received modulation signal, where v_{C} is the SM capacitor voltage and N is the number of FBSMs.

B. Single-Arm HSS Model of M^{3}C

This paper is focused on the modelling of M^{3}C under balanced grid conditions, while its modelling under unbalanced grid conditions is left for future research. Due to the symmetry of both the circuit topology of M^{3}C and the external conditions, only the model of arm au is established to reduce the model scale as well as the computation burden.

Based on Kirchhoff Voltage Law (KVL), the circuit equation of M^{3}C single-arm au can be established as:

$$\frac{\mathrm{d}i_{\mathrm{au}}}{\mathrm{d}t}=\frac{1}{L}(e_{\mathrm{u}}-v_{\mathrm{au}}-e_{\mathrm{a}}-v_{\mathrm{n}}-Ri_{\mathrm{au}}) \tag{21}$$

where e_{u}, e_{a}, are the voltages of phase-terminal u and a, respectively; i_{au}, v_{au} are the arm current and SM-stack output voltage of arm au, respectively; L, R is the arm of inductance and resistance, respectively; v_{n} is the voltage between the neutral points of the two sides; If the zero-sequence grid voltages on both sides are negligible, v_{n} equals the average of the arm output voltages:

$$v_{\mathrm{n}}=-\frac{1}{9}\sum_{i\in a,b,c}^{j\in u,v,w}v_{ij} \tag{22}$$

Considering the inner-arm FBSM energy balancing control, the capacitor voltages in the same arm are assumed equal for simplicity. Under this assumption, the single-arm voltage of M^{3}C can be described as:

$$v_{\mathrm{au}}=Nm_{\mathrm{au}}v_{\mathrm{Cau}} \tag{23}$$

where m_{au} and v_{Cau} are arm modulation signal and average SM capacitor voltage of arm au, respectively.

In addition, by ignoring the parameter deviation between the submodules, the dynamic of the SM capacitor voltage can be expressed as:

$$\frac{\mathrm{d}v_{\mathrm{Cau}}}{\mathrm{d}t}=\frac{1}{C}m_{\mathrm{au}}i_{\mathrm{au}} \tag{24}$$

where C is the SM capacitance.

Based on (21)–(24), the state-space model of the single-arm au of M^{3}C can be established by utilizing v_{Cau} and i_{au} as the state variables, e_{u} and e_{a} as the input variables, which is expressed as:

$$s\boldsymbol{x}_{\mathrm{cqt}}^{\mathrm{org}}(t)=\boldsymbol{A}_{\mathrm{cqt}}^{\mathrm{org}}(t)\boldsymbol{x}_{\mathrm{cqt}}^{\mathrm{org}}(t)+\boldsymbol{B}_{\mathrm{cqt}}^{\mathrm{org}}(t)\boldsymbol{u}_{\mathrm{cqt}}^{\mathrm{org}}(t) \tag{25}$$

where the subscript cqt represents the single-arm circuit model; the superscript org represents the original mathematical model before the HSS expansion.

$$\boldsymbol{x}_{\mathrm{cqt}}^{\mathrm{org}}(t)=[v_{\mathrm{Cau}}(t)\quad i_{\mathrm{au}}(t)]^{\mathrm{T}},\ \boldsymbol{u}_{\mathrm{cqt}}^{\mathrm{org}}(t)=[e_{\mathrm{u}}(t)\quad e_{\mathrm{a}}(t)]^{\mathrm{T}} \tag{26}$$

$$\boldsymbol{A}_{\mathrm{cqt}}^{\mathrm{org}}(t)=\begin{bmatrix}0 & \frac{m_{\mathrm{au}}(t)}{C}\\ -\frac{Nm_{\mathrm{au}}(t)}{L_{\mathrm{eq}}} & -\frac{R}{L_{\mathrm{eq}}}\end{bmatrix},\ \boldsymbol{B}_{\mathrm{cqt}}^{\mathrm{org}}(t)=\begin{bmatrix}0 & 0\\ \frac{1}{L_{\mathrm{eq}}} & -\frac{1}{L_{\mathrm{eq}}}\end{bmatrix} \tag{27}$$

To facilitate subsequent analysis, the model needs to be further linearized around the steady-state operation point. The small-signal models of the M^{3}C can be expressed as follows:

$$\begin{aligned}\Delta\dot{\boldsymbol{x}}_{\mathrm{cqt}}^{\mathrm{org}}(t)=&\boldsymbol{A}_{\mathrm{cqt}}^{\mathrm{orgS}}\Delta x_{\mathrm{cqt}}^{\mathrm{org}}(t)+\boldsymbol{B}_{\mathrm{cqt}}^{\mathrm{orgS}}\Delta\boldsymbol{u}_{\mathrm{cqt}}^{\mathrm{org}}(t)\\&+\Delta\boldsymbol{A}_{\mathrm{cqt}}^{\mathrm{org}}(t)\boldsymbol{x}_{\mathrm{cqt}}^{\mathrm{orgS}}\end{aligned} \tag{28}$$

where the superscript S represents the steady-state value of the corresponding variable; Δ represents the small-signal disturbance near the steady-state value. The third term $\Delta\boldsymbol{A}_{\mathrm{cqt}}^{\mathrm{org}}(t)x_{\mathrm{cqt}}^{\mathrm{S}}$ is used to model the effect of the control system on the modulation signals during disturbance.

To maintain cohesion with the control system model, the third term in (28) is rewritten as the small-signal expression:

$$\Delta\boldsymbol{A}_{\mathrm{cqt}}^{\mathrm{org}}(t)\boldsymbol{x}_{\mathrm{cqt}}^{\mathrm{orgS}}=\boldsymbol{W}_{\mathrm{ctl}}^{\mathrm{orgS}}\Delta\boldsymbol{y}_{\mathrm{ctl}}(t) \tag{29}$$

$$\boldsymbol{W}_{\mathrm{ctl}}^{\mathrm{orgS}}=\begin{bmatrix}\frac{i_{\mathrm{au}}^{\mathrm{S}}}{C} & -\frac{Nv_{\mathrm{Cau}}^{\mathrm{S}}}{L_{\mathrm{eq}}}\end{bmatrix}^{\mathrm{T}},\ \Delta\boldsymbol{y}_{\mathrm{ctl}}(t)=\Delta m_{\mathrm{au}}(t) \tag{30}$$

where the subscript ctl represents the model of control system; $\Delta\boldsymbol{y}_{\mathrm{ctl}}$ denotes the modulation signals.

In the steady state is an LTP system, and v_{C} and i_{au} are periodically time-varying making it difficult to carry out further investigation.

In this regard, the HSS modelling method transforms (28) into a Linear time-invariant (LTI) model. Based on the dual-fundamental-frequency HSS model can be established via the method in proposed Section II, which is expressed as:

$$\begin{aligned}s\Delta\boldsymbol{X}_{\mathrm{cqt}}=&(\boldsymbol{A}_{\mathrm{cqt}}^{\mathrm{S}}-\boldsymbol{N}_{\mathrm{cqt}})\Delta\boldsymbol{X}_{\mathrm{cqt}}+\boldsymbol{B}_{\mathrm{cqt}}^{\mathrm{S}}\Delta\boldsymbol{U}_{\mathrm{cqt}}\\&+\boldsymbol{W}_{\mathrm{ctl}}^{\mathrm{S}}\Delta\boldsymbol{Y}_{\mathrm{ctl}}\end{aligned} \tag{31}$$

where the mathematical forms of $\Delta\boldsymbol{X}_{\mathrm{cqt}}$, $\Delta\boldsymbol{U}_{\mathrm{cqt}}$ and $\Delta\boldsymbol{Y}_{\mathrm{ctl}}$ are the same as in (14) and (15), and the n^{th}-order submatrices are shown in (26), respectively:

$$\Delta\boldsymbol{x}_{\mathrm{cqt},(k_1,k_2)}=[\Delta v_{\mathrm{Cau}(k_1,k_2)}\quad \Delta i_{\mathrm{au}(k_1,k_2)}]^{\mathrm{T}}$$
$$\Delta\boldsymbol{u}_{\mathrm{cqt},(k_1,k_2)}=[\Delta e_{\mathrm{u}(k_1,k_2)}\quad \Delta e_{\mathrm{a}(k_1,k_2)}]^{\mathrm{T}}$$

$$\Delta \boldsymbol{y}_{\mathrm{ctl},(k_1,k_2)} = \Delta m_{\mathrm{au}(k_1,k_2)} \tag{32}$$

$\boldsymbol{A}^{\mathrm{S}}_{\mathrm{cqt}}$, $\boldsymbol{W}^{\mathrm{S}}_{\mathrm{cqt}}$, and $\boldsymbol{B}^{\mathrm{S}}_{\mathrm{cqt}}$ are of the formation shown in (18), and the $(k_1^{\mathrm{th}}, k_2^{\mathrm{th}})$-order submatrices are shown in (33)–(35), respectively:

$$\boldsymbol{A}^{\mathrm{S}}_{\mathrm{cqt},(k_1,k_2)} = \begin{cases} \begin{bmatrix} 0 & m^{\mathrm{S}}_{\mathrm{au},(k_1,k_2)}/C \\ 0 & -R/L_{\mathrm{eq}} \end{bmatrix} (k_1 = 0 \& k_2 = 0) \\ \begin{bmatrix} 0 & m^{\mathrm{S}}_{\mathrm{au},(k_1,k_2)}/C \\ -N m^{\mathrm{S}}_{\mathrm{au},(k_1,k_2)}/L_{\mathrm{eq}} & 0 \end{bmatrix} (k_1, k_2 \neq 0) \end{cases} \tag{33}$$

$$W^{\mathrm{S}}_{\mathrm{ctl},(k_1,k_2)} = \begin{cases} \begin{bmatrix} i^{\mathrm{S}}_{\mathrm{au},(k_1,k_2)}/C & 0 \end{bmatrix}^{\mathrm{T}} (k_1 = 0 \& k_2 = 0) \\ \begin{bmatrix} i^{\mathrm{S}}_{\mathrm{au},(k_1,k_2)}/C \\ -N v^{\mathrm{S}}_{\mathrm{Cau},(k_1,k_2)}/L_{\mathrm{eq}} \end{bmatrix} (k_1, k_2 \neq 0) \end{cases} \tag{34}$$

$$\boldsymbol{B}^{\mathrm{S}}_{\mathrm{cqt},(k_1,k_2)} = \begin{cases} \frac{1}{L_{\mathrm{eq}}} \begin{bmatrix} 0 & 0 \\ 1 & -1 \end{bmatrix} (k_1 = 0 \& k_2 = 0) \\ \boldsymbol{O}_{2\times 2}, (k_1, k_2 \neq 0) \end{cases} \tag{35}$$

where $\boldsymbol{O}_{2\times 2}$ represents a 2×2 zero matrix; L_{eq} represents the equivalent inductance of the arm current determined by the flowing path of specific current component. The arm current can be divided into four categories [15]:

1) the system-side-tied or LF-side-tied, whose $L_{\mathrm{eq}} = L/3$;
2) the circulating components whose $L_{\mathrm{eq}} = L$;
3) the zero-sequence flowing-through component, whose $L_{\mathrm{eq}} = \infty$ due to blocked zero-sequence current path.

C. HSS Modelling of the M^{3}C Control System.

Figure 5 shows the block diagram of the control system of M^{3}C. The control system of M^{3}C generally follows the classic architecture of the voltage source converter. The hierarchy structure is generally utilized containing three links: the outer loop, inner loop, and modulation. The outer loop is responsible for regulating the input and output reactive power while maintaining the long-term energy balance, which outputs the current reference for the inner loop. The inner loop is responsible for controlling the current to track the reference value issued by the outer loop and outputting the desired arm voltages to the modulation link, which can be divided into three parts: system-side current control, LF-side current control and circulating current suppression. The modulation link is responsible for generating the trigger signal of each submodule. This paper is focused on the harmonic characteristics below 300 Hz, and the dynamic of the modulation link is fast enough to be ignored. Consequently, only the outer loop and inner loop are considered.

1) Outer Loop

Without any loss of generality, the system side is set to maintain the energy balance of the M^{3}C and regulate the reactive power. In contrast, the LF-side is set to regulate the active and reactive power. The outer loop control equations can be expressed as:

$$\begin{bmatrix} i^{\mathrm{ref}}_{\mathrm{S}d} \\ i^{\mathrm{ref}}_{\mathrm{S}q} \end{bmatrix} = \left(K_{\mathrm{P\_So}} + \frac{K_{\mathrm{I\_So}}}{s} \right) \begin{bmatrix} v^{\mathrm{ref}}_{\mathrm{C}} - v_{\mathrm{C00}} \\ Q^{\mathrm{ref}}_{\mathrm{S}} - Q_{\mathrm{S}} \end{bmatrix} \tag{36}$$

$$\begin{bmatrix} i^{\mathrm{ref}}_{\mathrm{L}d} \\ i^{\mathrm{ref}}_{\mathrm{L}q} \end{bmatrix} = \left(K_{\mathrm{P\_Lo}} + \frac{K_{\mathrm{I\_Lo}}}{s} \right) \begin{bmatrix} P^{\mathrm{ref}}_{\mathrm{L}} - P_{\mathrm{L}} \\ Q^{\mathrm{ref}}_{\mathrm{L}} - Q_{\mathrm{L}} \end{bmatrix} \tag{37}$$

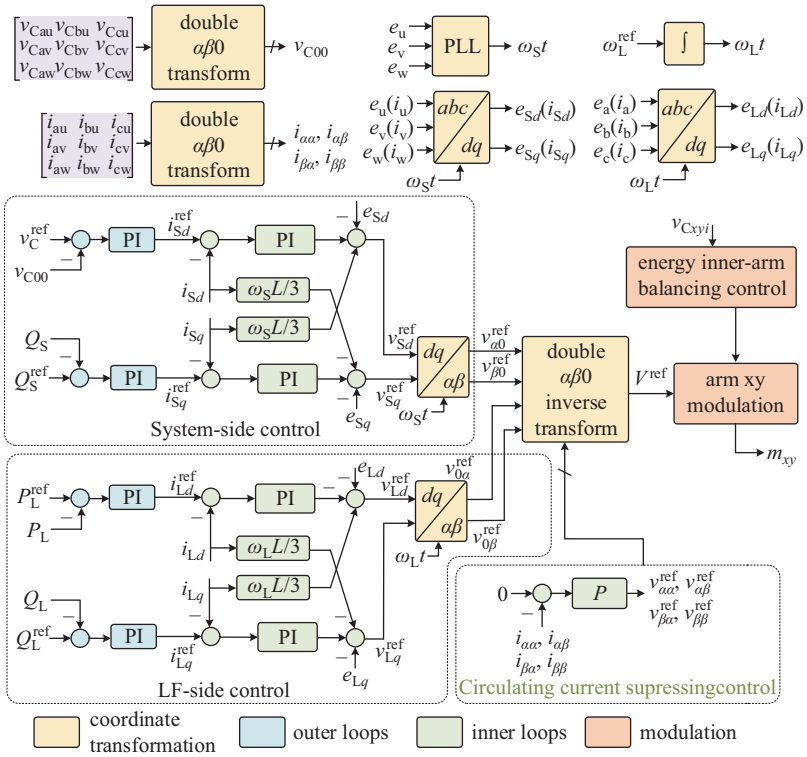

Fig. 5. Overview of the control system of M^{3}C.

where the superscript ref represents the reference value of the corresponding variable; $K_{\mathrm{P\_So}}$ and $K_{\mathrm{I\_So}}$ represents the PI gain of the outer loop controller on the system side, respectively; $K_{\mathrm{P\_Lo}}$ and $K_{\mathrm{I\_Lo}}$ represents the PI gain of the outer loop controller on the LF-side, respectively; Q_{S}, P_{L}, and Q_{L} represents the reactive power output on system-side, the active power and reactive power output on LF-side, respectively.

2) Inner Loop

The inner loop can be divided into system-side, LF-side current controller, and circulating current suppression controller (CCSC). In terms of the former two controllers, the M^{3}C has similar current dynamics on both sides, and the grid-tied current is controlled under the corresponding synchronous frame. The control equation is expressed by:

$$\begin{aligned}\begin{bmatrix} v_{\mathrm{S}d}^{\mathrm{ref}} \\ v_{\mathrm{S}q}^{\mathrm{ref}} \end{bmatrix} &= \left(K_{\mathrm{P\_Si}} + \frac{K_{\mathrm{I\_Si}}}{s}\right)\left(\begin{bmatrix} i_{\mathrm{S}d}^{\mathrm{ref}} \\ i_{\mathrm{S}q}^{\mathrm{ref}} \end{bmatrix} - \begin{bmatrix} i_{\mathrm{S}d} \\ i_{\mathrm{S}q} \end{bmatrix}\right) \\ &\quad + \begin{bmatrix} e_{\mathrm{S}d} \\ e_{\mathrm{S}q} \end{bmatrix} + \frac{\omega_{\mathrm{S}} L}{3}\begin{bmatrix} i_{\mathrm{S}q} \\ -i_{\mathrm{S}d} \end{bmatrix} \end{aligned} \tag{38}$$

$$\begin{aligned}\begin{bmatrix} v_{\mathrm{L}d}^{\mathrm{ref}} \\ v_{\mathrm{L}q}^{\mathrm{ref}} \end{bmatrix} &= \left(K_{\mathrm{P\_Li}} + \frac{K_{\mathrm{I\_Li}}}{s}\right)\left(\begin{bmatrix} i_{\mathrm{L}d}^{\mathrm{ref}} \\ i_{\mathrm{L}q}^{\mathrm{ref}} \end{bmatrix} - \begin{bmatrix} i_{\mathrm{L}d} \\ i_{\mathrm{L}q} \end{bmatrix}\right) + \begin{bmatrix} e_{\mathrm{L}d} \\ e_{\mathrm{L}q} \end{bmatrix} \\ &\quad + \frac{\omega_{\mathrm{L}} L}{3}\begin{bmatrix} i_{\mathrm{L}d} \\ -i_{\mathrm{L}q} \end{bmatrix} \end{aligned} \tag{39}$$

where $v_{\mathrm{S}d}^{\mathrm{ref}}/v_{\mathrm{S}q}^{\mathrm{ref}}$ and $v_{\mathrm{L}d}^{\mathrm{ref}}/v_{\mathrm{L}q}^{\mathrm{ref}}$ represents the output of the inner current loop controller on the system and LF-side, respectively; $i_{\mathrm{S}d}^{\mathrm{ref}}/i_{\mathrm{S}q}^{\mathrm{ref}}$ and $i_{\mathrm{L}d}^{\mathrm{ref}}/i_{\mathrm{L}q}^{\mathrm{ref}}$ represents the output of the outer loop controller on the system and LF-side, respectively; $i_{\mathrm{S}d}/i_{\mathrm{S}q}$ and $i_{\mathrm{L}d}/i_{\mathrm{L}q}$ represents the feedback current of the corresponding grid-connected circuit, respectively; $K_{\mathrm{P\_Si}}/K_{\mathrm{P\_Li}}$ and $K_{\mathrm{I\_Si}}/K_{\mathrm{I\_Li}}$ represents the PI gain of the inner loop controller.

On the contrary, the CCSC is placed on the double-$\alpha\beta 0$ stationary frame. The circulating current components can be extracted via the double-$\alpha\beta 0$ transformation:

$$\begin{bmatrix} i_{\alpha\alpha} & i_{\beta\alpha} & i_{0\alpha} \\ i_{\alpha\beta} & i_{\beta\beta} & i_{0\beta} \\ i_{\alpha 0} & i_{\beta 0} & i_{00} \end{bmatrix} = \boldsymbol{T}_{\alpha\beta 0}\begin{bmatrix} i_{\mathrm{au}} & i_{\mathrm{bu}} & i_{\mathrm{cu}} \\ i_{\mathrm{av}} & i_{\mathrm{bv}} & i_{\mathrm{cv}} \\ i_{\mathrm{aw}} & i_{\mathrm{bw}} & i_{\mathrm{cw}} \end{bmatrix}\boldsymbol{T}_{\alpha\beta 0}^{\mathrm{T}} \tag{40}$$

where $i_{\alpha\alpha}$, $i_{\beta\alpha}$, $i_{\alpha\beta}$, and $i_{\beta\beta}$ denote the circulating current components. Due to the many frequency components in $i_{\alpha\alpha}$, $i_{\beta\alpha}$, $i_{\alpha\beta}$, and $i_{\beta\beta}$, as well as the strong coupling effect between them, the CCSC utilizes the proportional control to achieve wide spectrum circulating current suppression, i.e.:

$$\begin{bmatrix} v_{\alpha\alpha}^{\mathrm{ref}} & v_{\beta\alpha}^{\mathrm{ref}} \\ v_{\alpha\beta}^{\mathrm{ref}} & v_{\beta\beta}^{\mathrm{ref}} \end{bmatrix} = -K_{\mathrm{CCSC}}\begin{bmatrix} i_{\alpha\alpha} & i_{\beta\alpha} \\ i_{\alpha\beta} & i_{\beta\beta} \end{bmatrix} \tag{41}$$

where K_{CCSC} represents the proportional gain of the CCSC.

Similarly, the voltage references on the *dq* frame are converted back to the double-$\alpha\beta 0$ frame via:

$$\begin{bmatrix} v_{\alpha 0}^{\mathrm{ref}} \\ v_{\beta 0}^{\mathrm{ref}} \end{bmatrix} = \boldsymbol{T}_{dq,\omega_{\mathrm{S}}}^{-1}\begin{bmatrix} v_{\mathrm{S}d}^{\mathrm{ref}} \\ v_{\mathrm{S}q}^{\mathrm{ref}} \end{bmatrix},\ \begin{bmatrix} v_{0\alpha}^{\mathrm{ref}} \\ v_{0\beta}^{\mathrm{ref}} \end{bmatrix} = -\boldsymbol{T}_{dq,\omega_{\mathrm{L}}}^{-1}\begin{bmatrix} v_{\mathrm{L}d}^{\mathrm{ref}} \\ v_{\mathrm{L}q}^{\mathrm{ref}} \end{bmatrix} \tag{42}$$

The voltage references on the double-$\alpha\beta 0$ frame are finally converted back to the individual arm voltage references via:

$$\begin{bmatrix} v_{\mathrm{au}}^{\mathrm{ref}} & v_{\mathrm{bu}}^{\mathrm{ref}} & v_{\mathrm{cu}}^{\mathrm{ref}} \\ v_{\mathrm{av}}^{\mathrm{ref}} & v_{\mathrm{bv}}^{\mathrm{ref}} & v_{\mathrm{cv}}^{\mathrm{ref}} \\ v_{\mathrm{aw}}^{\mathrm{ref}} & v_{\mathrm{bw}}^{\mathrm{ref}} & v_{\mathrm{cw}}^{\mathrm{ref}} \end{bmatrix} = \boldsymbol{T}_{\alpha\beta 0}^{-1}\left(\begin{bmatrix} v_{\alpha\alpha}^{\mathrm{ref}} & v_{\beta\alpha}^{\mathrm{ref}} & v_{0\alpha}^{\mathrm{ref}} \\ v_{\alpha\beta}^{\mathrm{ref}} & v_{\beta\beta}^{\mathrm{ref}} & v_{0\beta}^{\mathrm{ref}} \\ v_{\alpha 0}^{\mathrm{ref}} & v_{\beta 0}^{\mathrm{ref}} & v_{00}^{\mathrm{ref}} \end{bmatrix}\right)(\boldsymbol{T}_{\alpha\beta 0}^{-1})^{\mathrm{T}} \tag{43}$$

where v_{xy}^{ref} represents the voltage reference in arm xy.

At last, the modulation signals can be expressed as:

$$\begin{bmatrix} m_{\mathrm{au}} & m_{\mathrm{bu}} & m_{\mathrm{cu}} \\ m_{\mathrm{av}} & m_{\mathrm{bv}} & m_{\mathrm{cv}} \\ m_{\mathrm{aw}} & m_{\mathrm{bw}} & m_{\mathrm{cw}} \end{bmatrix} = \frac{1}{n v_{\mathrm{C}}^{\mathrm{ref}}}\begin{bmatrix} v_{\mathrm{au}}^{\mathrm{ref}} & v_{\mathrm{bu}}^{\mathrm{ref}} & v_{\mathrm{cu}}^{\mathrm{ref}} \\ v_{\mathrm{av}}^{\mathrm{ref}} & v_{\mathrm{bv}}^{\mathrm{ref}} & v_{\mathrm{cv}}^{\mathrm{ref}} \\ v_{\mathrm{aw}}^{\mathrm{ref}} & v_{\mathrm{bw}}^{\mathrm{ref}} & v_{\mathrm{cw}}^{\mathrm{ref}} \end{bmatrix} \tag{44}$$

3) HSS Model of the M^{3}C Controller

Based on (36)–(44) and linearization, the small-signal model of the M^{3}C controller can be established as:

$$\begin{cases} s\Delta\boldsymbol{x}_{\mathrm{ctl}} = \boldsymbol{A}_{\mathrm{ctl}}\Delta\boldsymbol{x}_{\mathrm{ctl}} + [\boldsymbol{B}_{\mathrm{ctl1}} \quad \boldsymbol{B}_{\mathrm{ctl2}} \quad \boldsymbol{B}_{\mathrm{ctl3}}]\begin{bmatrix} \Delta\boldsymbol{u}_{\mathrm{ctl1}} \\ \Delta\boldsymbol{u}_{\mathrm{ctl2}} \\ \Delta\boldsymbol{u}_{\mathrm{ctl3}} \end{bmatrix} \\ \Delta\boldsymbol{y}_{\mathrm{ctl}} = \boldsymbol{C}_{\mathrm{ctl}}\Delta\boldsymbol{x}_{\mathrm{ctl}} + [\boldsymbol{D}_{\mathrm{ctl1}} \quad \boldsymbol{D}_{\mathrm{ctl2}} \quad \boldsymbol{D}_{\mathrm{ctl13}}]\begin{bmatrix} \Delta\boldsymbol{u}_{\mathrm{ctl1}} \\ \Delta\boldsymbol{u}_{\mathrm{ctl2}} \\ \Delta\boldsymbol{u}_{\mathrm{ctl3}} \end{bmatrix} \end{cases} \tag{45}$$

where $\Delta\boldsymbol{x}_{\mathrm{ctl}}$ denotes the state variables of the outer/inner loops; the input vector $\Delta\boldsymbol{u}_{\mathrm{ctl}}$ is divided into three parts to facilitate further derivation: $\Delta\boldsymbol{u}_{\mathrm{ctl1}}$ for the reference values of SM capacitor voltage and grid-side powers, $\Delta\boldsymbol{u}_{\mathrm{ctl2}}$ for the boundary grid voltages, and $\Delta\boldsymbol{u}_{\mathrm{ctl3}}$ for the measured arm currents and SM capacitor voltages. Correspondingly, the coefficient matrices of $\Delta\boldsymbol{B}_{\mathrm{ctl}}$ and $\Delta\boldsymbol{D}_{\mathrm{ctl}}$ are also divided.

Similarly, the (45) is expanded via the proposed hold. All the vectors and matrices share the dual-expanded HSS format as shown in (14) to (18). The bottom sub-vectors and sub-matrices can be derived based on the time-domain control equations.

$$\begin{aligned}\Delta\boldsymbol{x}_{\mathrm{ctl}(k_1,k_2)} = [&\Delta x_{1(k_1,k_2)} \quad \Delta x_{2(k_1,k_2)} \quad \Delta x_{3(k_1,k_2)} \\ &\Delta x_{4(k_1,k_2)}]^{\mathrm{T}}\end{aligned} \tag{46}$$

$$\Delta\boldsymbol{u}_{\mathrm{ctl1}(k_1,k_2)} = \begin{cases} [v_{\mathrm{C}}^{\mathrm{ref}} \quad Q_{\mathrm{S}}^{\mathrm{ref}} \quad P_{\mathrm{L}}^{\mathrm{ref}} \quad Q_{\mathrm{L}}^{\mathrm{ref}}]^{\mathrm{T}}, & k_1 = 0 \& k_2 = 0 \\ \boldsymbol{O}_{4\times 1}, & \text{otherwise} \end{cases} \tag{47}$$

$$\Delta\boldsymbol{u}_{\mathrm{ctl2}(k_1,k_2)} = \Delta u_{\mathrm{cqt},(k_1,k_2)} \tag{48}$$

$$\Delta\boldsymbol{u}_{\mathrm{ctl3},(k_1,k_2)} = \Delta x_{\mathrm{cqt},(k_1,k_2)} \tag{49}$$

Subsequently, by combining (45) and (31), Fig. 6 shows the detailed integrating process of circuit model and control model; the HSS model of single-arm au with close-loop control can be established as:

$$\begin{aligned}\begin{bmatrix} s\Delta\boldsymbol{X}_{\mathrm{cqt}} \\ s\Delta\boldsymbol{X}_{\mathrm{ctl}} \end{bmatrix} &= \begin{bmatrix} \boldsymbol{A}_{\mathrm{cqt}}^{\mathrm{S}} - \boldsymbol{N}_{\mathrm{cqt}} + \boldsymbol{W}_{\mathrm{ctl}}^{\mathrm{S}}\boldsymbol{D}_{\mathrm{ctl3}} & \boldsymbol{W}_{\mathrm{ctl}}^{\mathrm{S}}\boldsymbol{C}_{\mathrm{ctl}} \\ \boldsymbol{B}_{\mathrm{ctl3}} & \boldsymbol{A}_{\mathrm{ctl}} - \boldsymbol{N}_{\mathrm{ctl}} \end{bmatrix}\begin{bmatrix} \Delta\boldsymbol{X}_{\mathrm{cqt}} \\ \Delta\boldsymbol{X}_{\mathrm{ctl}} \end{bmatrix} \\ &\quad + \begin{bmatrix} \boldsymbol{B}_{\mathrm{cqt}}^{\mathrm{S}} + \boldsymbol{W}_{\mathrm{ctl}}^{\mathrm{S}}\boldsymbol{D}_{\mathrm{ctl2}} & \boldsymbol{W}_{\mathrm{ctl}}^{\mathrm{S}}\boldsymbol{D}_{\mathrm{ctl1}} \\ \boldsymbol{B}_{\mathrm{ctl2}} & \boldsymbol{B}_{\mathrm{ctl1}} \end{bmatrix}\begin{bmatrix} \Delta\boldsymbol{U}_{\mathrm{cqt}} \\ \Delta\boldsymbol{U}_{\mathrm{ctl1}} \end{bmatrix}\end{aligned} \tag{50}$$

which is further abbreviated as:

$$s\Delta\boldsymbol{X}_{\mathrm{syn}} = \boldsymbol{A}_{\mathrm{syn}}\Delta\boldsymbol{X}_{\mathrm{syn}} + \boldsymbol{B}_{\mathrm{syn}}\Delta\boldsymbol{U}_{\mathrm{syn}} \tag{51}$$

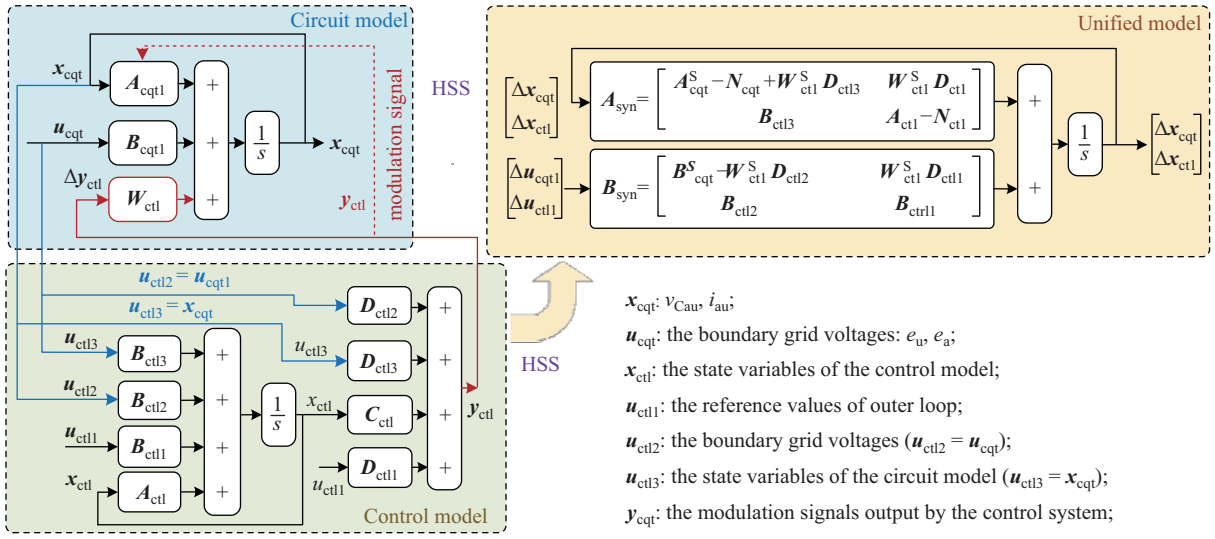

Fig. 6. The schematic diagram of integrating circuit model and control model.

where the subscript syn represents the M^{3}C HSS model considering the closed-loop controller.

IV. Harmonic Coupling Analysis

The dual-expanded small-signal HSS model can be utilized in a variety of research, such as impedance modelling, stability research, *etc.* This paper is focused on the steady-state harmonic coupling characteristics between the system side and the LF-side. The small-signal HSS model of M^{3}C includes the panoramic coupling information between all the frequency components inner and out of M^{3}C, and to analyze the harmonic coupling characteristics of the boundary and internal variables, the MIMO harmonic transmission function is established.

Firstly, the output of the model is selected as all the frequency components contained in i_{au} and v_{Cau}, i.e.:

$$\Delta \boldsymbol{Y}_{\mathrm{syn}} = \boldsymbol{C}_{\mathrm{syn}}[\Delta \boldsymbol{X}_{\mathrm{cqt}} \quad \Delta \boldsymbol{X}_{\mathrm{ctl}}]^{\mathrm{T}} \tag{52}$$

$$\boldsymbol{C}_{\mathrm{syn}} = \begin{bmatrix} \mathrm{diag}(1 \quad \cdots \quad 1 \quad \cdots \quad 1) & \boldsymbol{O}_{\mathrm{cqt}} \\ \boldsymbol{O}_{\mathrm{cqt}}^{\mathrm{T}} & \boldsymbol{O}_{\mathrm{ctl}} \end{bmatrix} \tag{53}$$

Then, the harmonic transfer function $\boldsymbol{H}$ can be established as:

$$\boldsymbol{H} = \boldsymbol{C}_{\mathrm{syn}}(s\boldsymbol{I} - \boldsymbol{A}_{\mathrm{syn}})^{-1}\boldsymbol{B}_{\mathrm{syn}} \tag{54}$$

By letting $s = 0$ in (54), the harmonic admittance matrix between the M^{3}C arm current harmonics and the grid-side voltages on the steady-state can be obtained. In the obtained matrix, each element denotes the coupling gain between the corresponding input-output pair. The non-zero elements in $\boldsymbol{H}$ reflect the harmonic coupling relationship between the arm current and the external voltages, while the amplitudes represent the coupling strength.

The M^{3}C with parameters in Table I is utilized as the benchmark, and the 5$^{\mathrm{th}}$-order truncated HSS model is established. Fig. 7(a), (b), (c) and (d) show the harmonic coupling gains of v_{Cau}, i_{au}, i_{u}, i_{a} to e_{a}, respectively, where the x-axis is the dual-dimensional spectrum following the displacement rule of dual-fundamental-frequency vectors shown in (29) and (30), which is separated into 11 sections according to the order on the ω_{S} dimension.

TABLE I
Parameters of the M^{3}C Benchmark

Parameter	Value	Unit
System-side grid voltage	220	kV
System-side fundamental grid frequency	50	Hz
LF-side grid voltage	220	kV
LF-side fundamental grid frequency	20	Hz
Arm resistance	1	Ω
Arm inductance	10	mH
Rated SM capacitor voltage	3	kV
SM capacitance	3	mF
Number of SMs per arm	150	–
PI gain of average SM capacitor voltage loop	[3, 100]	–
PI gain of system-side current loop	[40, 1000]	–
PI gain of LF-side current loop	[15, 500]	–
PI gain of circulating current loop	300	–

It can be concluded from Fig. 7 that:

1) In Fig. 7(a) and (b), the coupling gains are centro-symmetrically distributed on the dual-fundamental-frequency panel. This is because the HSS model is derived on the complex frequency domain, and therefore, the conjugated pair of elements have identical amplitude.

2) In Fig. 7(a) and (b), given a (0, n_Δ)-order disturbance voltage on the LF-side, it will cause ($\pm\Delta k_{\mathrm{S}}, n_\Delta \pm \Delta k_{\mathrm{L}}$)-order current harmonic, and $[\pm\Delta k_{\mathrm{S}}, n_\Delta \pm (\Delta k_{\mathrm{L}} + 1)]$-order capacitor voltage ripple, where Δk_{S}, $\Delta k_{\mathrm{L}} = 1, 3, 5, \cdots$. The amplitudes tend to become smaller as the harmonic order increases because the SM capacitance and arm inductance have a stronger filtering effect at higher frequencies.

3) To investigate the grid-side harmonic coupling characteristics, the components contained in i_{a} and i_{u} are extracted in Fig. 7(c) and (d), respectively. Therefore, Fig. 7(c) shows the harmonic coupling relationship on the same side, while Fig. 7(d) shows the harmonic coupling relationship between the two sides.

4) In Fig. 7(c), the amplitudes are the largest along the main diagonal axis and tend to decrease away from it. The

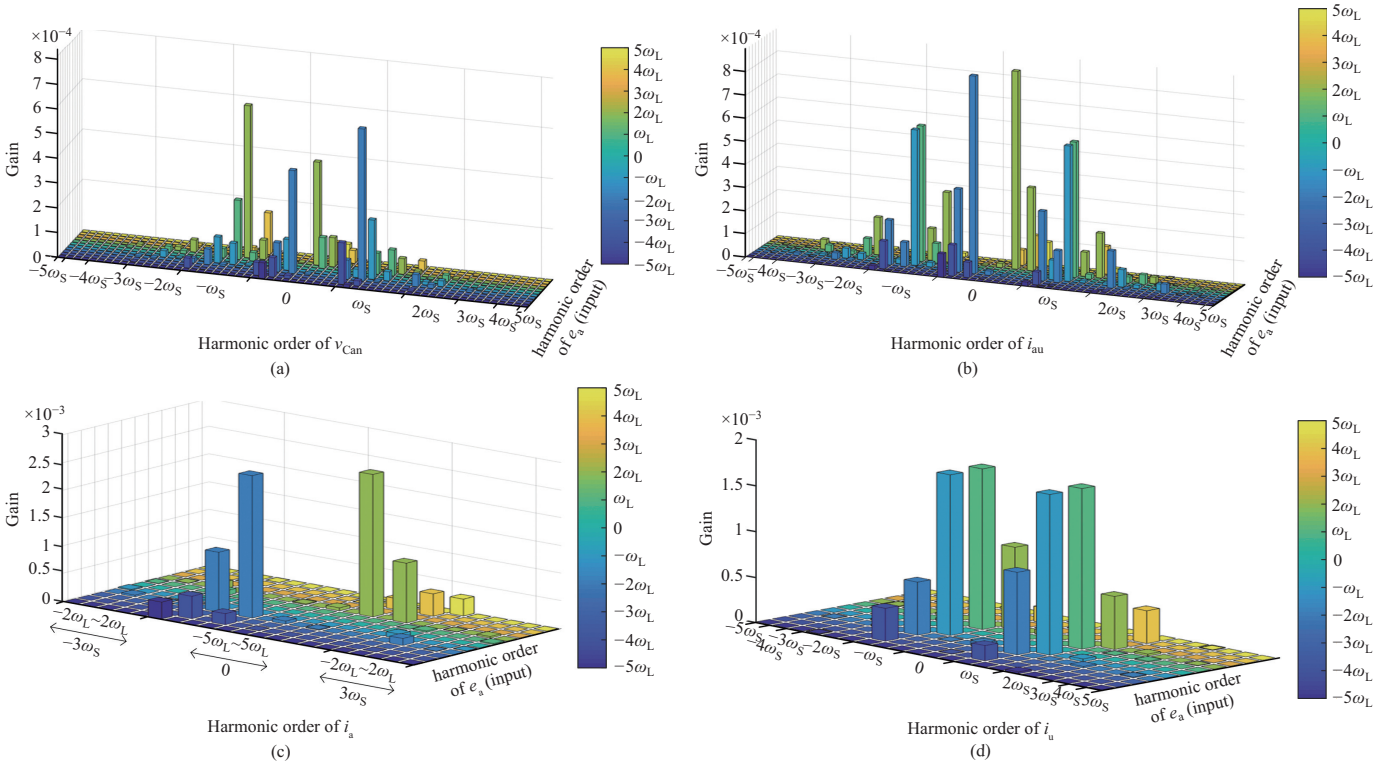

Fig. 7. Harmonic coupling gains of the M^{3}C. (a) Between v_{Cau} and e_{a}. (b) Between i_{au} and e_{a}. (c) Between i_{a} and e_{a}. (d) Between i_{u} and e_{a}.

largest ones correspond to the equivalent impedance, where the input and output have the same frequency. However, other elements still have considerable amplitudes, which indicates that the inner dynamics will arouse cross-frequency harmonic coupling. That is, given a $(0, n_\Delta)$-order positive (negative) sequence disturbance voltage on the LF-side, it will cause the $(0, n_\Delta)$-order positive(negative)-sequence current harmonic, and the $(0, n_\Delta \pm 2)$-order negative (positive)-sequence current harmonic on the LF-side. This conclusion can also be extended to the system side.

5) Fig. 7(d) shows that an unignorable coupling relationship exists between the system-side current and LF-side voltage. Given a $(0, n_\Delta)$-order sequence disturbance voltage on the LF-side, it will cause the $(\pm\Delta k_{\mathrm{S}}, n_\Delta \pm \Delta k_{\mathrm{L}})$-order current harmonic on the system side. This conclusion can also be extended to the system side, where $n_\Delta + \Delta k_{\mathrm{L}} = 3k$; k, Δk_{S}, $\Delta k_{\mathrm{L}} = 1, 3, 5, \cdots$. This conclusion can also be extended to the relationship between system-side voltage and LF-side current.

V. Simulation Verification and Discussion

To verify the correctness and effectiveness of the proposed method and established model, this section compares the dynamic and steady-state output results of the established HSS model (HM) and electromagnetic transient simulation (TM) model. The results of the two methods are compared in Fig. 8.

Figure 8(a) shows the output results of the HSS model under different truncation orders and simulation models. The SM capacitor voltage v_{Cau} and the arm current i_{au} are highly consistent with the electromagnetic transient simulation results, and the accuracy will become higher with the increase of the truncation order. To further verify the correctness of the model, Fig. 8(b) and Appendix present each frequency component obtained from the HM under different truncation orders and compare them with their counterparts from the TM. For the frequency components covered by the model, i.e., the $2f_{\mathrm{L}}$, $2f_{\mathrm{S}}$ and $(f_{\mathrm{S}} \pm f_{\mathrm{L}})$ components contained in v_{Cau}, and the f_{L}, f_{S}, $(f_{\mathrm{S}} \pm 2f_{\mathrm{L}})$ and $(2f_{\mathrm{S}} \pm f_{\mathrm{L}})$ components contained in i_{au}, are highly consistent with the TM results. However, the selection for truncation order will ignore the components with higher order. For example, the 4$^{\mathrm{th}}$-order and 5$^{\mathrm{th}}$-order components, such as the $(f_{\mathrm{S}} \pm 3f_{\mathrm{L}})$ components in v_{Cau}, are absent in the third order and contribute a considerable part to the 3$^{\mathrm{rd}}$-order model error.

Figure 8(c) and (d) show the error of the HM relative to the TM together with spectrum analysis under different truncation orders. The time-domain relative error of v_{Cau} and i_{au} under different truncation orders is shown in Table II. The maximum relative error of v_{Cau} and i_{au} are 2.84% and 3.11%, respectively. The errors are mostly truncation errors caused by uncovered frequency components, as has been analyzed before. Particularly, the error of the 3$^{\mathrm{rd}}$-order model mainly consists of the $(f_{\mathrm{S}} - 3f_{\mathrm{L}})$ (10 Hz) and $(2f_{\mathrm{S}} - 2f_{\mathrm{L}})$ (60 Hz) components in v_{Cau}, and the $(2f_{\mathrm{S}} - 3f_{\mathrm{L}})$ (40 Hz), $(f_{\mathrm{S}} - 4f_{\mathrm{L}})$ (110 Hz) and $(3f_{\mathrm{S}} + 2f_{\mathrm{L}})$ (190 Hz) components in i_{au}. In contrast, the error of the 5$^{\mathrm{th}}$-order model mainly consists of the $(2f_{\mathrm{S}} - 4f_{\mathrm{L}})$ (20 Hz) component in v_{Cau}, and the $(3f_{\mathrm{S}} - 4f_{\mathrm{L}})$ (70 Hz) component in i_{au}. However, these errors are significantly reduced with the increase in the truncation order. For example, the 10 Hz error in v_{Cau} decreases from 3.56 in the 3$^{\mathrm{rd}}$-order model to 0.10 in the 5$^{\mathrm{th}}$-order model, and 0.03 in the 7$^{\mathrm{th}}$-order model. Tables A3 and A4 in the Appendix provide

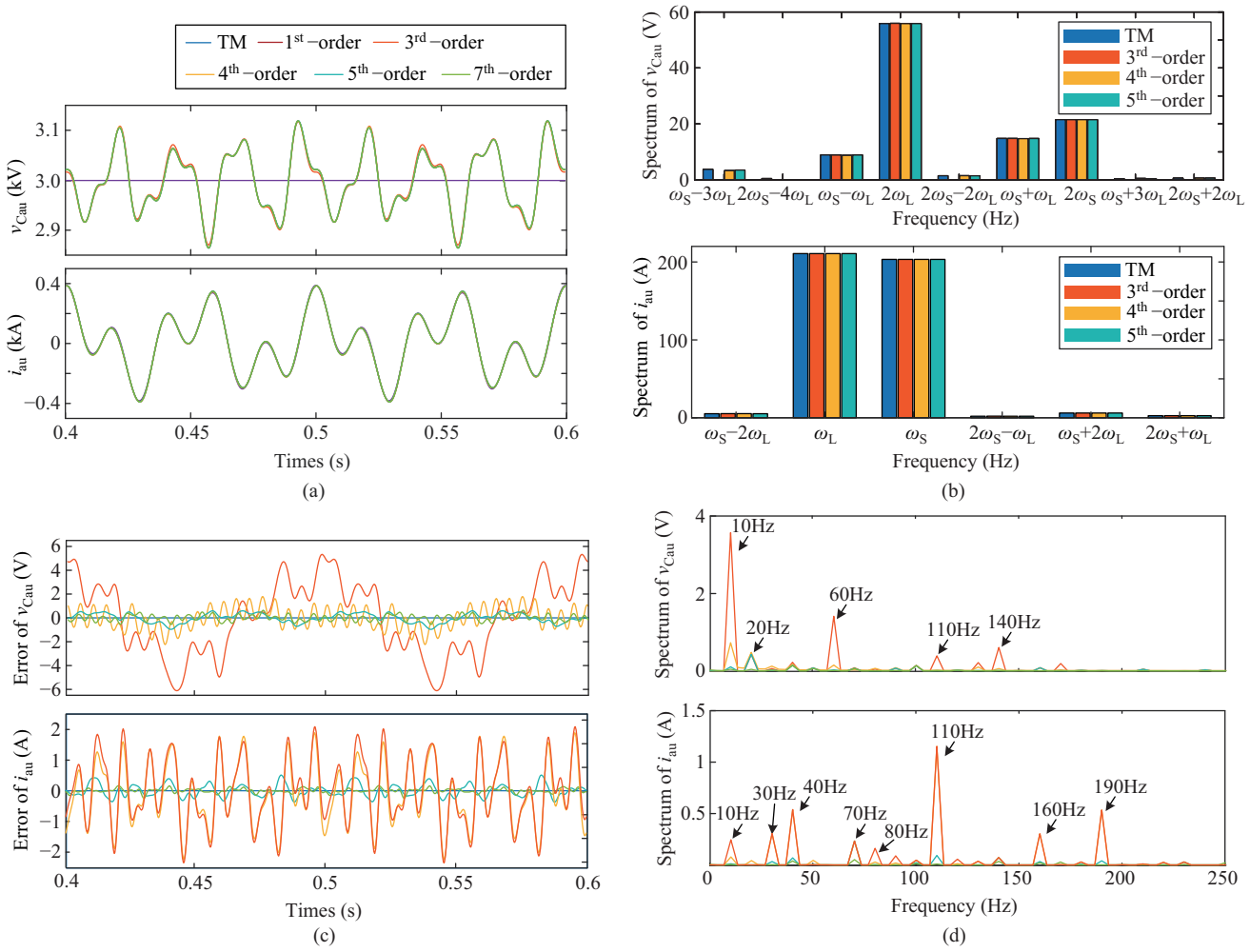

Fig. 8. Voltage and current waveforms. (a) Steady-state wave-forms of various orders. (b) Dominant harmonic amplitudes of various orders. (c) The error of v_{Cau} and i_{au}. (d) The error spectrum of v_{Cau} and i_{au}.

TABLE II
ANALYSIS OF v_{cau}'S AND i_{au}' S ERROR OBTAINED FROM THE HM COMPARED WITH THE TM

	1		3		4		5		7	
	MAE	MRE (%)	MAE	MRE (%)	MAE	MRE (%)	MAE	MRE (%)	MAE	MRE (%)
v_{Cau}	87.725	2.84	4.921	0.159	1.657	0.053	0.550	0.018	0.505	0.016
i_{au}	13.117	3.11	2.089	0.498	2.073	0.494	0.511	0.122	0.166	0.039

a much more detailed error spectrum analysis. The frequency components of the error of the 3rd-order and 4th-order models are basically not reflected in the 5th-order model. In addition, compared with the error spectrum of v_{Cau} and i_{au}, the lower-frequency components of v_{Cau} are relatively high. The reason is that the control system of M^{3}C is equipped with a harmonic circulation suppression loop, which can effectively reduce the absolute amplitude of lower-frequency harmonic current; however, there is no corresponding suppression strategy for the lower-frequency capacitor voltage ripple of submodules. To conclude, the proposed dual-expanded HSS modelling method can accurately reflect the internal dynamic characteristics of M^{3}C under dual-fundamental-frequency electric coupling.

To verify the correctness of the established harmonic transmission matrix further quantitatively, this section injects perturbation voltage (16% p.u., 40 Hz) to the LF-side of the established models. The waveforms from the TM and HM are shown in Fig. 9(a). It can be seen the HM outputs are basically matching with the corresponding TM results with the perturbation voltage. Fig. 9(b) shows comparison results of the dominant bridge arm voltage ripple, bridge arm current harmonics and grid-side harmonics extracted from the TM and the 5th-order HM. When a 40 Hz AC perturbance voltage is injected into the LF-side, the 40 Hz and 80 Hz components are the dominant disturbance components on the LF-side.

In contrast, the 10 Hz and 110 Hz components are the dominant disturbance components on the system side, which is consistent with the conclusions of Fig. 7. The errors presented in Fig. 9(b) are mainly due to some frequency components not covered due to the low truncation order of the model, such as 20 Hz ($2f_{\mathrm{S}}-6f_{\mathrm{L}}$) and 50 Hz ($5f_{\mathrm{S}}-15f_{\mathrm{L}}$) of i_{u}. In addition, due to the dual-fundamental-frequency

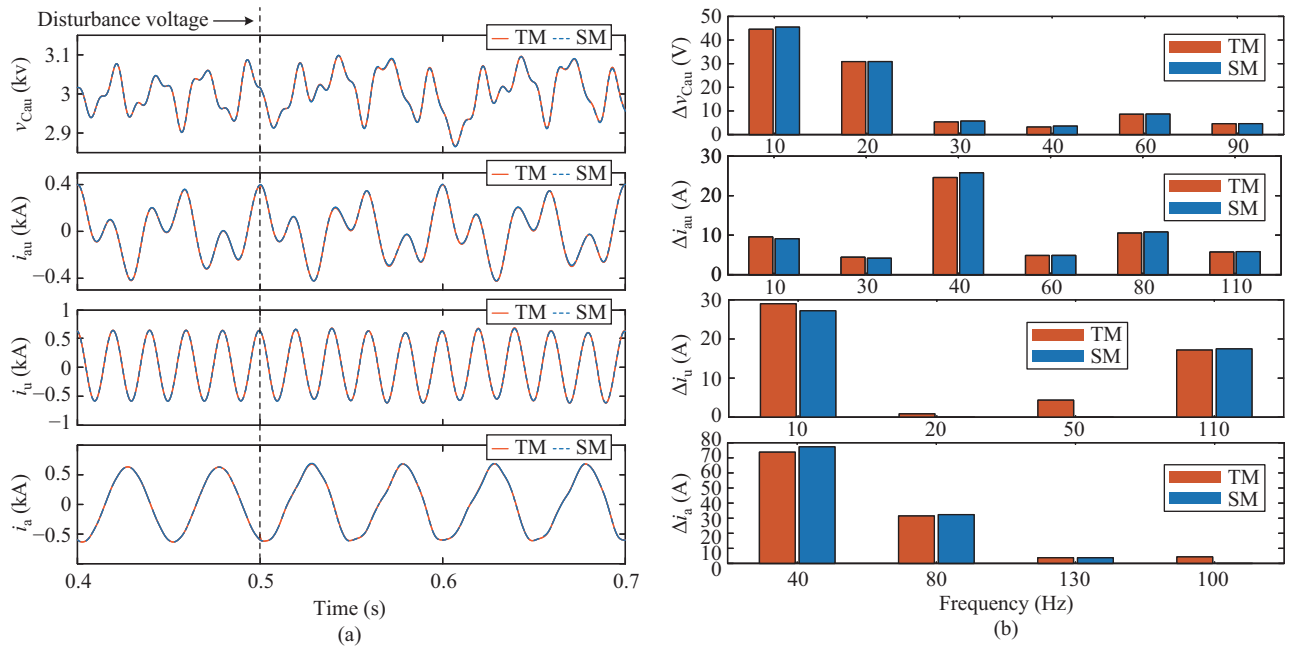

Fig. 9. Waveforms obtained with perturbation. (a) Comparison between steady-state waveforms obtained with TM and HM under perturbation voltage. (b) Comparison of dominant harmonica amplitudes between steady-state waveforms obtained with TM and HM under perturbation voltage.

coupling characteristics of M^{3}C and the proximity of the two fundamental frequencies, it will inevitably encounter the harmonic spectrum overlapping problem; that is, two different algebraically different frequencies are numerically close to or even coincide. For example, the 10 Hz component of i_u is the superposition of 4^{th}-order ($f_S - 3f_L$) and 17^{th}-order ($5f_S - 12f_L$) and many other possible combinations. However, the 17^{th}-order and other components are not reflected in the HM, which causes relatively large errors. This is the most remarkable characteristic that distinguishes M^{3}C from single-fundamental-frequency scenarios such as regular MMC in HVDC. More research on the solution to this problem will be presented in future research.

VI. Conclusion

This paper proposes a novel HSS modelling method to achieve high-order dynamics modelling considering internal harmonic coupling characters. It reveals the internal harmonic coupling relationship of M^{3}C and the net-side current harmonic transmission relationship. The following conclusions are drawn from this study.

1) The conventional high-order dynamic modelling method is not suitable for M^{3}C and other AC-AC direct frequency converter with dual-fundamental-frequency characteristics; the improved HSS modelling method can effectively solve the modelling issue of dual-fundamental-frequency characteristic systems.

2) The comparative results of the electromagnetic transient simulation under the same parameter show that the established model can better reflect the dynamic and steady-state characteristics of M^{3}C and verify the correctness of the improved HSS modelling method.

3) The proposed modelling method can effectively realize the mathematical description of the high-order dynamic process of the internal of M^{3}C, clearly depict the cross-coupling process between the state variables of different frequencies and different phase sequences and depict the influence of its output characteristics.

References

[1] S. Q. Liu, X. F. Wang, L. H. Ning, B. Y. Wang, M. Lu, and C. C. Shao, "Integrating offshore wind power via fractional frequency transmission system," *IEEE Transactions on Power Delivery*, vol. 32, no. 3, pp. 1253–1261, Jun. 2017.

[2] Y. Q. Meng, S. H. Yan, K. Wu, L. H. Ning, X. Li, X. L. Wang, and X. F. Wang, "Comparative economic analysis of low frequency ac transmission system for the integration of large offshore wind farms," *Renewable Energy*, vol. 179, pp. 1955–1968, Dec. 2021.

[3] Y. Wang, R. Wang, K. Tanaka, et al., "Accelerating the energy transition towards photovoltaic and wind in China," *Nature*, vol. 619, 2023.

[4] R. W. Erickson and O. A. Al-Naseem, "A new family of matrix converters," in *Proceedings of IECON'01. 27th Annual Conference of the IEEE Industrial Electronics Society*, 2001, pp. 1515–1520.

[5] J. J. Lou, K. Lin, J. N. Li, Y. Xue, and X. P. Zhang, "Cost analysis and comparison between modular multilevel converter (MMC) and modular multilevel matrix converter (M^{3}C) for offshore wind power transmission," in *Proceedings of 15th IET International Conference on AC and DC Power Transmission*, 2019, pp. 1–6.

[6] S. Q. Liu, X. F. Wang, B. Y. Wang, P. W. Sun, Q. Zhou, and Y. Cui, "Comparison between back-to-back MMC and M^{3}C as high power AC/AC converters," in *Proceedings of 2016 IEEE PES Asia-Pacific Power and Energy Engineering Conference*, 2016, pp. 671–676.

[7] B. Y. Wang, X. F. Wang S. Q. Liu, C. C. Shao, H. Y. Bai, W. P. Zhu, and Y. Y. Feng, "Reliability comparison of two types of converters for fractional frequency transmission system," in *Proceedings of 2016 IEEE PES Asia-Pacific Power and Energy Engineering Conference*, 2016, pp. 1627–1631.

[8] F. Kammerer, J. Kolb, and M. Braun, "A novel cascaded vector control scheme for the modular multilevel matrix converter," in *Proceedings of IECON 2011 - 37th Annual Conference of the IEEE Industrial Electronics Society*, 2011, pp. 1097–1102.

[9] F. Kammerer, J. Kolb, and M. Braun, "Fully decoupled current control and energy balancing of the modular multilevel matrix converter," in *Proceedings of 2012 15th International Power Electronics and Motion Control Conference*, 2012, pp. LS2a.3–1–LS2a.3–8.

[10] W. Kawamura, M. Hagiwara, and H. Akagi, "Control and experiment of a modular multilevel cascade converter based on triple-star bridge cells," *IEEE Transactions on Industry Applications*, vol.50, no.5, pp.3536–3548, Sept.-Oct. 2014.

[11] W. Kawamura, Y. Chiba, M. Hagiwara, and H. Akagi, "Experimental verification of an electrical drive fed by a modular multilevel TSBC converter when the motor frequency gets closer or equal to the supply frequency," *IEEE Transactions on Industry Applications*, vol. 53, no. 3, pp. 2297–2306, May-Jun. 2017.

[12] W. Kawamura, Y. Chiba, and H. Akagi, "A broad range of speed control of a permanent magnet synchronous motor driven by a modular multilevel TSBC converter," *IEEE Transactions on Industry Applications*, vol. 53, no. 4, pp. 3821–3830, Jul./Aug. 2017.

[13] J. J. Luo, X. P. Zhang, Y. Xue, K. H. Gu, and F. Wu, "Harmonic analysis of modular multilevel matrix converter for fractional frequency transmission system," *IEEE Transactions on Power Delivery*, vol. 35, no. 3, pp. 1209–1219, Jun. 2020.

[14] P. W. Sun, X. F. Wang, Y. S. Hu, C. X. Xie, and L. H. Ning, "The harmonic analysis and the arm capacitor parameters selection of module multilevel matrix converter," in *Proceedings of 2016 IEEE PES Asia-Pacific Power and Energy Engineering Conference*, 2016, pp. 1617–1621.

[15] S. Q. Liu, B. Y. Zhao, G. Wang, and X. F. Wang, "An improved phasor method for modelling and analysis of modular multilevel matrix converter," *IEEE Transactions on Power Delivery*, Vol. 36, no. 3, pp. 1744–1755, Jun. 2021.

[16] C. Luo, Q. Guo, Y. Hu, S. Y. Li, Y. H. Zhu, and H. P. Guo, "Analysis and countermeasures of harmonic instability in a practical HVDC system with fixed series compensation and STATCOM," *IEEE Transactions on Industry Applications*, vol. 59, no. 2, pp. 2509–2518, Mar.-Apr. 2023.

[17] Q. H. Wu, A. Bose, C. Singh; J. H. Chow, G. Mu and Y. Z. Sun, "Control and stability of large-scale power system with highly distributed renewable energy generation: viewpoints from six aspects," *CSEE Journal of Power and Energy Systems*, vol. 9, no. 1, pp. 8–14, Jan. 2023.

[18] L. S. Xiong, X. K. Liu, Y. H. Liu, and F. Zhuo, "Modeling and stability issues of voltage-source converter-dominated power systems: A review," *CSEE Journal of Power and Energy Systems*, vol. 8, no. 6, pp. 1530–1549, Nov. 2022.

[19] Ö. C. Sakinci and J. Beerten, "Equivalent multiple *dq*-frame model of the MMC using dynamic phasor theory in the $\alpha\beta z$-frame," *IEEE Transactions on Power Delivery*, vol. 35, no. 6, pp. 2916–2927, Dec. 2020.

[20] Ö. C. Sakinci and J. Beerten, "Generalized dynamic phasor modeling of the MMC for small-signal stability analysis," *IEEE Transactions on Power Delivery*, vol. 34, no. 3, pp. 991–1000, Jun. 2019.

[21] J. Lyu, X. Zhang, X. Cai, and M. Molinas, "Harmonic state-space based small-signal impedance modeling of a modular multilevel converter with consideration of internal harmonic dynamics," *IEEE Transactions on Power Electronics*, vol. 34, no. 3, pp. 2134–2148, Mar. 2019.

[22] J. Lyu, X. Zhang, J. J. Huang, J. W. Zhang, and X. Cai, "Comparison of harmonic linearization and harmonic state space methods for impedance modeling of modular multilevel converter," in *Proceedings of 2018 International Power Electronics Conference*, 2018, pp. 1004–1009.

[23] Z. G. Xu, B. B. Li, L. J. Han, J. L. Hu, S. B. Wang, S. G. Zhang, and D. G. Xu, "A complete HSS-based impedance model of MMC considering grid impedance coupling," *IEEE Transactions on Power Electronics*, vol. 35, no. 12, pp. 12929–12948, Dec. 2020.

[24] J. J. Luo, X. P. Zhang, and Y. Xue, "Small signal model of modular multilevel matrix converter for fractional frequency transmission system," *IEEE Access*, vol. 7, pp. 110187–110196, Jul. 2019.

[25] X. F. Wang and F. Blaabjerg, "Harmonic stability in power electronic-based power systems: concept, modeling, and analysis," *IEEE Transactions on Smart Grid*, vol. 10, no. 3, pp. 2858–2870, May 2019.

[26] Y. C. Liao and X. F. Wang, "Small-signal modeling of AC power electronic systems: critical review and unified modeling," *IEEE Open Journal of Power Electronics*, vol. 2, pp. 424–439, Aug. 2021.

[27] J. H. Zhu, Z. R. Guo, J. B. Hu, S. C. Ma, and J. B. Guo, "Truncation number selection of harmonic state-space model based on the floquet characteristic exponent," *IEEE Transactions on Industrial Electronics*, vol. 70, no. 3, pp. 3222–3228, Mar. 2023.

Jing Li received the M.S. degrees in Power Systems and Their Automation from South China University of Technology, Guangzhou, China, in 2023. He is currently studying in Xi'an Jiaotong University for his Ph.D. degree. His current research interests include novel power transmission schemes and control of renewable energy systems.

Boyang Zhao received the B.S., M.S. and Ph.D degrees in Electrical Engineering from Xi'an Jiaotong University, Xi'an, China, in 2015, 2018 and 2023, respectively. He also received the Engineer's degree (Diplôme d'Ingénieur) from CentraleSupélec, Gif-sur-Yvette, France, in 2018. He is currently an Assistant Professor in Electrical Engineering, Xi'an Jiaotong University. His current research interests include novel power transmission schemes and control of renewable energy systems.

Shenquan Liu received the Ph.D. degree in Electrical Engineering from Xi'an Jiaotong University, Xi'an, China, in 2018. From 2016 to 2017, he was a Visiting Student at the School of Electrical and Computer Engineering, Georgia Institute of Technology, Atlanta, GA, USA. In 2018, he was a Research Associate at the Department of Electrical Engineering, The Hong Kong Polytechnic University, Hong Kong, China. He is currently a Postdoctoral Research Fellow with the Department of Electrical Engineering, South China University of Technology, Guangzhou, China. His current research interests include HVDC, novel power transmission approaches, and FACTS.

Jie Li received a B.E. degree in Electrical Engineering from Beijing Jiaotong University, Beijing, China, in 2016, and a Ph.D. degree in Power Systems and Their Automation from South China University of Technology, Guangzhou, China, in 2021. Currently, he is a Postdoctoral Research Fellow with South China University of Technology, Guangzhou, China. His research interests include protection and control for distribution networks.

Xiuli Wang received the B.S., M.S. and Ph.D. degrees in Electrical Engineering from Xi'an Jiaotong University, Xi'an, China, in 1982, 1985 and 1997, respectively. She has been with Xi'an Jiaotong University since 1985, where she is currently a Professor with School of Electrical Engineering. Her research interests include the power market, reliability assessment of power system and integration of renewable power.

Xifan Wang received the bachelor's degree in Electrical Engineering from Xi'an Jiaotong University, Xi'an, China, in 1957. From 1983 to 1986, he was a Visiting Scientist with Cornell University, Ithaca, NY, USA. From 1991 to 1994, he was a Visiting Professor with the Kyushu Institute of Technology, Kitakyushu, Japan. He is currently a Member of the Chinese Academy of Science, Beijing, China. He is currently the Director of the Research Institute of Power Systems, Xi'an Jiaotong University. His current research interests include the analysis, operation and planning of power systems, and novel transmission schemes.